

HIGH-POWER HARD X-RAY BEAM POSITION MONITOR DEVELOPMENT AT THE APS*

B.X. Yang, G. Decker, S. H. Lee, and P. Den Hartog
Advanced Photon Source, Argonne National Laboratory, Argonne, IL 60439, USA

Abstract

Accurate and stable x-ray beam position monitors (XBPMs) are key elements in a feedback control system for good x-ray beam stability. For the low-emittance mode of operation of the Advanced Photon Source (APS), the cross sections of the undulator x-ray beams are not upright ellipses, and the effective beam sizes in the horizontal and vertical planes depend on the undulator gaps. These beam characteristics introduce strong gap dependence in photo-emission blade-type XBPMs designed for upright elliptical beams. A center-of-mass XBPM will significantly reduce the gap dependence of the BPM readings. We report the development status of a high-power center-of-mass XBPM at the APS. We note that users often discard more than 50% of the undulator beam power outside of the monochromatic beam. These photons can be intercepted by the limiting aperture of the beamline, and their x-ray fluorescence footprint can be imaged onto a detector. The position of the x-ray beam can be read out using position-sensitive photodiodes. Thermal analyses show that the XBPM can be used for the measurement of beam with a total power up to 21 kW for the 7-GeV APS beam.

INTRODUCTION

X-ray beam stability is an important requirement from the Advanced Photon Source (APS) users. X-ray beam position monitors (XBPMs) are at the heart of the control system delivering the required stability. As the stability requirements become increasingly demanding, XBPMs are asked to deliver increasingly precise information about the x-ray beam. In this work, we propose a design concept that combines the function of a high-heat-load photon collimator and the beam position monitor. We will present a thermal analysis of the collimator, an optical design of the readout detector, and the results of preliminary tests.

XBPM Challenge

Table 1 shows properties of typical APS undulator sources, as well as the beam stability currently achieved and planned for the future upgrade [1].

Since its commissioning, the APS has used the photoemission blade-based XBPM [2]. It is located well away from the undulator beam core and does not have to handle the full power of the undulator under normal conditions. The thermal distortion of its blades has not been measured experimentally. The dependence of its calibration on undulator gap is its main weakness. To understand the gap dependence, let us consider a vertical XBPM using Gaussian beam approximation: We assume that the spatial distribution of the photoelectron is given by:

$$J_{PE}(y) = J_{PE0} e^{-(y-y_0)^2/2\sigma_y^2}, \quad (1)$$

where y_0 is the center of the x-ray beam. We further assume that the upper blade covers b to $+\infty$, and its signal is given by $I_{PE+} = \int_b^{\infty} J_{PE}(y) dy$. A similar expression can be written for the lower blade, $I_{PE-} = \int_{-\infty}^{-b} J_{PE}(y) dy$.

Table 1: XBPM Characteristics

Location (m)	Current	Planned
Maximum beam current	100	200
No. of Undulator A	1	2
Maximum power	6 kW	21 kW
Maximum power density	183 kW/mr ²	630 kW/mr ²
RMS stability, Horizontal	5 μ m/0.85 μ r	3 μ m/0.53 μ r
(0.1 – 200 Hz) Vertical	2 μ m/0.8 μ r	0.4 μ m/0.2 μ r

The BPM ratio signal is defined as the ratio of the difference over sum of these two signals,

$$R_{PE}(y_0) = \frac{\operatorname{erfc}\left(\frac{b-y_0}{\sqrt{2}\sigma_y}\right) - \operatorname{erfc}\left(\frac{b+y_0}{\sqrt{2}\sigma_y}\right)}{\operatorname{erfc}\left(\frac{b-y_0}{\sqrt{2}\sigma_y}\right) + \operatorname{erfc}\left(\frac{b+y_0}{\sqrt{2}\sigma_y}\right)}, \quad (2)$$

where $\operatorname{erfc}(u) = \frac{2}{\sqrt{\pi}} \int_u^{\infty} e^{-t^2} dt$ is the complementary error function. The readout of the BPM is given by $Y = l_y R_{PE}$, where the calibration length,

$$l_y = \sqrt{\frac{\pi}{2}} \sigma_y e^{\frac{b^2}{2\sigma_y^2}} \operatorname{erfc}\left(\frac{b}{\sqrt{2}\sigma_y}\right), \quad (3)$$

is chosen so $Y \approx y_0$ for small displacement. Figure 1 plots the calibration length l_y as a function of the beam size σ_y , for $b = 2, \dots, 6$ (mm). For fixed blade spacing, l_y depends on beam sizes: the larger the beam size, the larger is l_y , and the less sensitive the XBPM becomes.

When undulator harmonic energies are away from Au absorption edges, the broadband excitation can be approximated using bend magnet (BM) spectra. The total electron yield (TEY) from the gold surface can be estimated using Henke approximation [3] with x-ray spectra calculated with XOP [4]. We found that, as shown in Figure 2, the vertical TEY profile fits well to a pseudo-Student distribution function,

$$S_e = S_{e0} \left(1 + \frac{1}{\nu} \left| \frac{y_0}{\sigma_s} \right|^m \right)^{-\frac{\nu+1}{2}}, \quad (4)$$

* Work supported by U.S. Department of Energy, Office of Science, Office of Basic Energy Sciences, under Contract No. DE-AC02-06CH11357.

where m , ν , σ_x are parameters dependent on the critical energy of the BM source. This function gives the standard Student distribution when $m = 2$ [5].

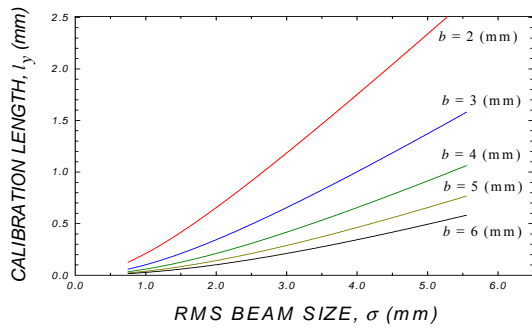


Figure 1: The BPM calibration length vs. Gaussian beam size σ_y for $b = 2, \dots, 6$ (mm).

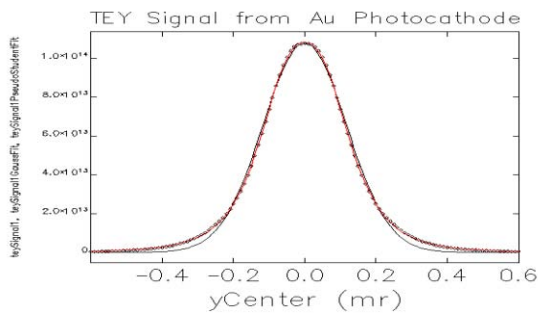


Figure 2: Calculated vertical gold TEY profile of BM source (circles), and a pseudo-Student fit (red line).

As an undulator gap changes, its effective critical energy changes, causing the width and shape of the vertical x-ray beam profile to change. As a consequence, the calibration length of the XBPM changes with the undulator gap. These changes are even more dramatic when one of the harmonics is near an absorption edge. Since the beam size is several mm, even a 1% change of the beam size is in the range of several tens of μm .

Figure 1 also reveals that for fixed beam sizes, the larger the blade spacing, the shorter the calibration length, and the BPM is more sensitive to beam movements. This encourages the practice to place blades away from the beam core, $b > \sigma_y$. As a result, the signal is significantly reduced (note that $\text{erfc}(1) = 16\%$ and $\text{erfc}(2) = 0.5\%$) and the background from bend magnet is significantly increased. At the APS, clean blade signals are hard to obtain for gaps wider than 30 mm.

Finally, the low-emittance lattice at the APS introduces horizontal and vertical dispersions and dispersion slopes within insertion devices. When the electron beam with energy spread passes through the undulator, it generates an x-ray beam with tilted cross sections, making the vertical TEY signal depend on the horizontal offset of the blades from the beam center.

GRAZING INCIDENCE XBPM

Discussions in the last section leads us to conclude that the best way to increase the signal-to-noise ratio is to maximize the undulator x-ray flux intercepted and minimize the background radiation received. This naturally leads to the solution of combining the XBPM

with the limiting aperture of the front end. Most collimator designs use copper alloys, hence copper K-edge x-ray fluorescence (Cu-K XRF) may be used for XBPM readout. Since the XRF footprint size is usually about half of TEY's, the XRF-XBPM is more sensitive to beam position changes. Figure 3 shows the vertical XRF profile measured at the APS diagnostics undulator [6] using a pair of slits and a silicon PIN diode monitoring the XRF from the beam dump. The profile fits well to a pseudo-Gaussian form,

$$S_f = S_{f0} e^{-\frac{1}{2} \left| \frac{y_0}{\sigma_m} \right|^m}, \quad (5)$$

with $\sigma_m = 1.6$ mm and $m = 2.73$. This functional form agrees well with calculations using a bend magnet source, where the parameters σ_m and m depend on the critical energy of the source. For undulators, they depend on the undulator gap.

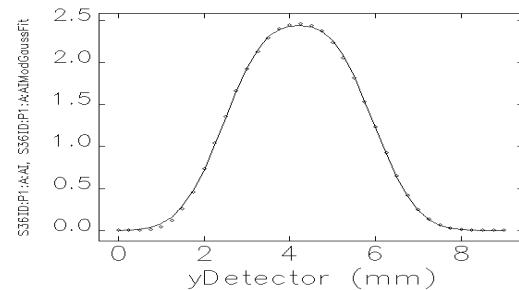


Figure 3: Measured vertical XRF profile of the APS diagnostics undulator from a Cu beam dump (circles) with a pseudo-Gaussian fit (line).

Table 2: RMS Beam Sizes for Diagnostics Undulator

Parameter	Location	Horizontal	Vertical
E-beam size	0 m	270 μm	12 μm
E-beam divergence	0 m	11.5 μr	4 μr
Mono x-ray beam size	20 m	0.36 mm	0.11 mm
	30 m	0.45 mm*	0.17 mm*
Cu XRF footprint size	20 m	0.9 mm	0.8 mm
	40 m	1.7 mm	1.6 mm**
Au TEY footprint	20 m	1.84 mm	1.82 mm
Power envelope	20 m	0.88 mm	0.84 mm

* Measured at 30 m from APS diagnostics undulator [6].

** Measured at 40 m from APS diagnostics undulator.

Table 2 lists the electron and x-ray beam sizes of the APS diagnostics undulator. The x-ray beam sizes of the monochromatic APS diagnostics undulator are measured using an x-ray wire scanner [7] at 30 m. They are consistent with the electron beam size and divergence derived from the lattice model. The measured values are extrapolated to the XBPM located at 20 m. The TEY and total power profile sizes are calculated using XOP.

Choice of Limiting Aperture for Undulator A

Table 3 lists the estimated x-ray beam sizes at 20 m from an APS Undulator A with a fully closed gap ($K = 2.6$). The properties of the e-beam are from Table 2. If the beam is centered in an aperture of $4\text{-}\sigma$ in both the horizontal and vertical sides, 1.6 mm (H) \times 0.5 mm (V), 99% of the monochromatic photons in the central zone would pass through the aperture. We choose 2 mm (H) \times

1 mm (V) to allow 0.5 mm missteering in both planes. Since the power and XRF envelopes are much wider than the mono beam size, the aperture intercepts about 75% of the total power and 70% of the total XRF intensity.

Table 3: Maximum Beam Sizes for Undulator A*

Parameter	Horizontal	Vertical
RMS Mono x-ray beam	0.36 mm	0.12 mm
RMS Cu XRF footprint	~ 2.2 mm	0.9 mm
RMS Au TEY footprint	~ 5.0 mm	2.0 mm
RMS X-ray power envelope	~ 2.4 mm	0.9 mm
Full x-ray aperture	2.0 mm	1.0 mm

* $K = 2.6, z = 20$ mm

Thermal Analysis

From Table 3, we can see that the power profile spreads wider horizontally than vertically. It was shown in studies of APS front end components that vertical surfaces of shutters and collimators are better for higher total power load applications [8]. Table 4 lists the design parameters of a new grazing incidence XBPM. Its active surface is made of cold-rolled GlidCop AL-15. ANSYS was used for the finite element thermal stress-strain analysis: Figure 4 shows the stress distribution over the GlidCop active surface. The temperature distribution looks similar. Figure 5 shows the temperature distribution over the cooling channel. Under operating conditions, the maximum cooling channel temperature, active surface temperature and Von-Mises stress will reach 77°C, 184°C and 296 MPa, respectively. Under the worst missteering conditions studied, they will reach 101°C, 229°C and 384 MPa, respectively. These values are well within our engineering limits of 150°C, 300°C and 455 MPa.

Table 4: Design Parameters for XBPM

Parameter	Value
Electron beam current	200 mA @ 7 GeV
Insertion device	2 Undulator A
Power load	21 kW
Max beam power density	1.68 kW/mm ²
X-ray grazing incidence angle	0.8°
Peak surface power density	23.5 W/mm ²
Heat transfer coefficient	0.010 W/mm ² /°C

Vertical beam position readout

The vertical position of the footprint is read out using a split silicon PIN diode and a slit-camera geometry, shown in Figure 6. The fluorescence signal produced by a source point at y in the lower diode is proportional to the illuminated area, $J_-(y) = C(a + My)$, where $M = S'/S$ is the magnification. For a distributed fluorescence source with an intensity distribution $\rho(y)$, we have $I_- = C \int \rho(y)(a + My) dy$. Similarly, we can write $I_+ = C \int \rho(y)(a - My) dy$. The BPM ratio is proportional to the center of mass (CM) coordinate of the distribution,

$$R(\bar{y}) = -\frac{I_+ - I_-}{I_+ + I_-} = \frac{M}{a} \frac{\int \rho(y) y dy}{\int \rho(y) dy} = \frac{M}{a} \bar{y}. \quad (6)$$

We note that the calibration length $l_y = a/M$. The higher the magnification, the more sensitive the XBPM is.

Instrumentation

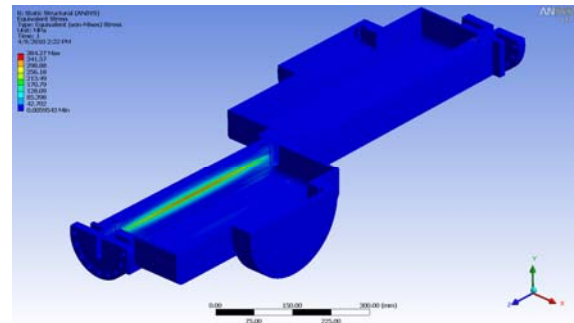


Figure 4: Stress distribution over the XBPM.

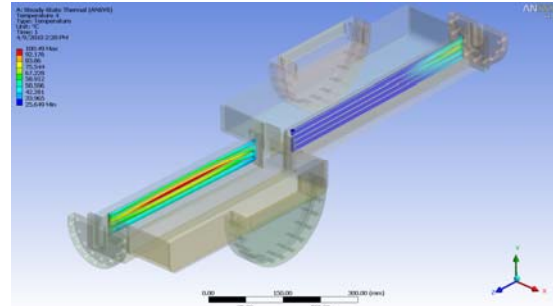


Figure 5: Cooling channel temperature distribution.

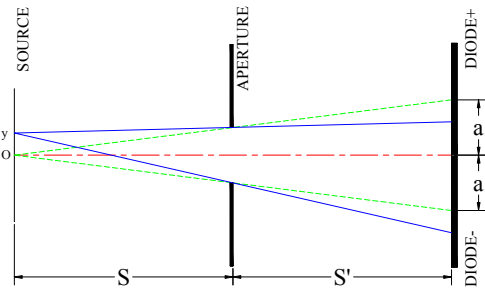


Figure 6: Vertical position readout: CM detector.

Horizontal Beam Position Readout

Due to artifacts we will discuss in the next section, it is more robust to derive the horizontal position from the total signal intensity from the left and right collimator plates. As discussed in the introduction, the horizontal ratio signal will depend on the effective beam size measured using XRF, which may be compensated using the following algorithm: Since the undulator beam size does not change when one reverses the magnetic field, we can write $\sigma_y^2 = \sigma_{y0}^2 (1 + b_2 K^2 + \dots)$. The signal intensity depends on undulator power, $I = I_0 K^2 (1 + c_2 K^2 + \dots)$. Combining the above expressions, we have

$$\sigma_y = \sigma_{y0} \sqrt{1 + a_2 \frac{I}{I_0} + a_4 \left(\frac{I}{I_0}\right)^2 + \dots} \quad (7)$$

This expression can be used to determine the vertical calibration length using Eq. (1), where b is the half aperture width. Other parameter, $\sigma_{y0}, I_0, a_2, \dots$, can be determined empirically from gap scan measurements.

MINIMIZING ARTIFACTS

The grazing incidence XBPM is susceptible to a number of known artifacts and others from imperfections.

Bend Magnet Radiation

The fringe of the bend magnet (BM) radiation reaches the XRF-XBPM, just as in the TEY-XBPM. However, due to higher threshold of excitation, $\epsilon_K = 8.98$ keV, soft x-ray radiation does not contribute to the XRF-XBPM signals, as long as the detector is properly filtered to block low-energy x-ray photons. A smaller acceptance aperture also helps to reduce BM background signal.

Powder Diffraction

Figure 7 shows measured powder diffraction peaks from the copper absorber, recorded with a narrow silicon PIN diode scanning above the water-cooled Cu beam stop. The x-ray beam was delivered by the APS diagnostics undulator (~ 24 keV) through a small aperture. Significant powder diffraction peaks (rings) can be seen at small angles. At lower photon energies from Undulator A, these peaks shift to higher angles and may enter the split PIN diode. When this happens, the additional photons make the source area of the diffraction peak appear to the detector as bright vertical stripes. Since the diffraction ring intensity varies little near the orbit plane, these stripes are uniform along the vertical direction and do not pose a big problem for vertical position readout. However they may shift the horizontal center of mass slightly as a diffraction ring enters or leaves the diode. On the other hand, using the intensity signal for horizontal position readout reduces the impact of powder diffraction rings. Further reduction may be achieved by modifying the edge of the detector and letting the diffraction ring gradually reach its maximum intensity.

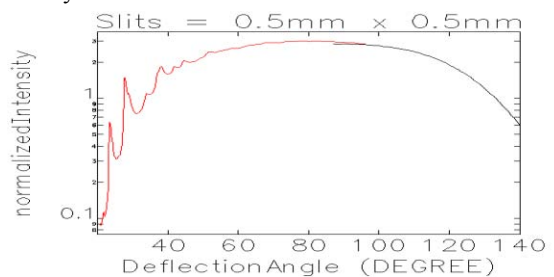


Figure 7: Power diffraction peak off the Cu absorber at 24 keV.

Compton Scattering

Compton scattering intensity from copper is strong. But its angular distribution is smooth and does not vary azimuthally. Hence its impact on position readouts is similar but less than powder diffraction.

Thermal bump

Figure 8 shows the thermal directional deformation of the active surface in the horizontal axis. We note overall deformation as well as longitudinal stretch of the collimator since the structure was supported via three kinematic points on the base surface, causing the asymmetric displacements around the baseline. In addition, the raised surface intercepts the x-ray photons

further upstream than the ideal planar surface, causing the center of weight to shift upstream, thus inducing error in CM measurements. If we use the intensity asymmetry as the position signal, the total intensity intercepted by the upstream plate determines the upstream signal, while the remainder is the downstream signal. In this scheme, maintaining the position of the edge of the upstream plate is critical. In Figure 8, $-21 \mu\text{m}$ of the total edge displacement of $-25 \mu\text{m}$ comes from the thermal and vacuum loads. If we instead support the collimator at its middle, the thermal bump would be dramatically reduced for the full 21 kW power load. We note that a horizontal missteering of 0.5 mm shifts the edge further by $-12 \mu\text{m}$. In practice, the latter appears as a horizontal calibration change of 12/500 and can be absorbed in Eq. (7). In summary, we expect the thermal bump to shift the origin at a level of $\sim 0.2 \mu\text{m}/\text{kW}$, which can be compensated with the diode signal.

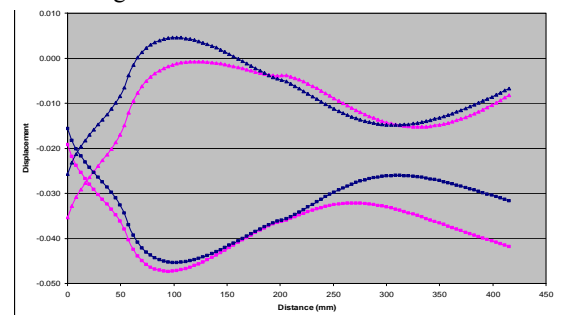


Figure 8: Thermally induced surface displacement.

Alignment Error

Due to the small grazing incidence angle, a minor misalignment may change the angle by a noticeable fraction, thus moving the fluorescence CM towards the mid-plane if the grazing incidence angle is increased, or away from it otherwise. This causes systematic errors if the CM was used for the horizontal signal. On the other hand, the fluorescence signal intensity is not very sensitive to the incidence angle, especially in a grazing geometry. The minor impact on the detected intensity of shifting XRF distribution can be further minimized if we use two or more split PIN diodes and position them along the z-direction at appropriate locations.

EXPERIMENTAL TEST

Figure 9 shows a schematic of the XBPM and figure 10 shows an in-air test setup for demonstrating the principle of the grazing incidence XBPM. It consists of a water-cooled copper split collimator as the absorber and two imaging detectors made of a horizontal slot and a silicon PIN diode assembly. The APS diagnostics undulator beamline, designed to accept the full undulator beam, was used to test the XBPM. The transverse calibration was performed by scanning the XY stages built in the XBPM support. Figure 11 shows vertical scan data for different undulator gaps. It can be seen that the gap dependence is well below $\pm 25 \mu\text{m}$ in these tests. Figure 12 shows horizontal scan data for different undulator gaps, showing a stronger gap-dependence, as expected from a sampling XBPM. Since the diagnostics undulator is a high-energy low-power device, these tests are limited in scope. We are

not able to quantify the effect for an undulator harmonic to cross the Cu K-edge, nor can we study the impact for a major power diffraction ring to pass the PIN diode. Furthermore, the permanent distortion due to thermal expansion hysteresis will not be studied until the XBPM is installed in an Undulator A front end.

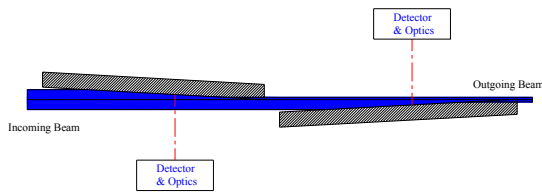


Figure 9: Schematic of the grazing incidence XBPM.

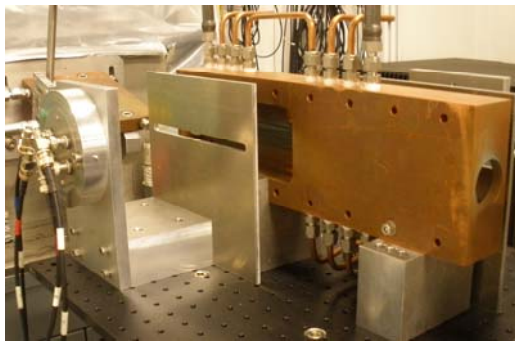


Figure 10: A test setup to demonstrate the grazing incidence XBPM sign principle.

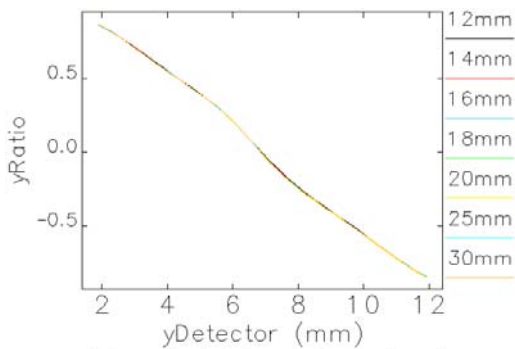


Figure 11: Vertical XBPM scan data for several undulator gaps.

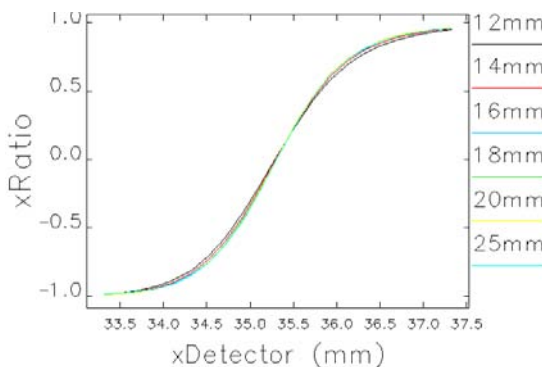


Figure 12: Horizontal XBPM scan data for several undulator gaps.

SUMMARY

We propose to combine the functions of the limiting aperture and an XBPM in the APS ID front ends and discuss one design to illustrate the concept. A vertical wall absorber was chosen for its power-bearing capacities; slit-camera geometry was chosen to read the vertical CM position of the fluorescence footprint. The horizontal position is derived from signal imbalance between two opposing absorbers to minimize the impacts of angular alignment error, thermal bumps, and x-ray powder diffraction. Gap-dependent compensation for horizontal readout is discussed. A preliminary test successfully demonstrated the validity of the principle.

REFERENCES

- [1] G. Decker, "APS beam Stability Studies at the 100-nanoradian Level," these proceedings.
- [2] D. Shu, B. Rodricks, J. Barraza, T. Sanchez, and T. M. Kuzay, "The APS x-ray undulator photon beam position monitor and tests at CHESS and NSLS," Nucl. Instrum. Methods, A 319, 56 (1992).
- [3] B. L. Henke, J. A. Smith, and D. T. Attwood, "0.1-10-keV x-ray-induced electron emissions from solids-Models and secondary electron measurements," J. Appl. Phys. 1852 (48) 1977.
- [4] M. Sanchez del Rio and R. J. Dejus, "Status of XOP: an x-ray optics software toolkit," SPIE Proceedings Vol. 5536 (2004) pp.171-174.
- [5] Jay L. Devore, *Probability and Statistics for Engineering and the Sciences*, 7th ed. Brooks and Cole, Belmont, CA, (2007).
- [6] B. X. Yang, A. H. Lumpkin, G. A. Goepfner, S. Sharma, E. Rotela, I. C. Sheng, E. Moog, "Status of the APS Diagnostics Undulator Beamline," PAC'97, 8P045, p. 2207 (1997); <http://www.JACoW.org>.
- [7] B. Yang, E. E. Norum, S. Shoaf, and J. Stevens, "X-ray Wire Scanner," these proceedings.
- [8] Y. Jaski, "New front-end design for multiple in-line undulators at the Advanced Photon Source," AIP Conf. Proc. 705, 356 (2004).